Available online at www.sciencedirect.com
SCIENCE DIRECT®
International Journal of Heat and Mass Transfer 48 (2005) 1662–1674
International Journal of HEAT and MASS TRANSFER
www.elsevier.com/locate/ijhmt

Microscale heat transfer enhancement using thermal boundary layer redeveloping concept

J.L. Xu [a,*], Y.H. Gan [a,b], D.C. Zhang [c], X.H. Li [c]

[a] *Guangzhou Institute of Energy Conversion, Chinese Academy of Sciences, Nengyuan Road, Wushan, Guangzhou 510640, PR China*
[b] *Department of Thermal and Energy Engineering, University of Science and Technology of China, Hefei 230027, Anhui Province, PR China*
[c] *Institute of Microelectronics, Peking University, Beijing, 100871, PR China*

Received 18 May 2004; received in revised form 6 December 2004

Abstract

We demonstrated a new silicon microchannel heat sink, composing of parallel longitudinal microchannels and several transverse microchannels, which separate the whole flow length into several independent zones, in which the thermal boundary layer is in developing. The redeveloping flow is repeated for all of the independent zones thus the overall heat transfer is greatly enhanced. Meanwhile, the pressure drops are decreased compared with the conventional microchannel heat sink. Both benefits of enhanced heat transfer and decreased pressure drop ensure the possibility to use "larger" hydraulic diameter of the microchannels so that less pumping power is needed, which are attractive for high heat flux chip cooling. The above idea fulfilled in microscale is verified by a set of experiments. The local chip temperature and Nusselt numbers are obtained using a high resolution Infrared Radiator Imaging system. Preliminary explanation is given on the decreased pressure drop while enhancing heat transfer. The dimensionless control parameter that guides the new heat sink design and the prospective of the new heat sink are discussed.

1. Introduction

In macroscale heat transfer can be enhanced by interrupting the boundary layer formation and providing more surface area. Louvered fins are examples to fulfill such heat transfer enhancement in the compact heat exchanger designs, which are widely used in several industry applications [1,2]. The available experimental/numerical studies show that the new boundary layer formation along the fin surface can have higher heat transfer coefficients [1]. In this paper we use the thermal boundary layer redeveloping concept in microscale and propose a new design of the silicon-based microchannel array with transversal channels.

As an example shown in Fig. 1, the new microchannel heat sink consists of ten parallel longitudinal triangular microchannels and five transverse trapezoid microchannels, which separate the whole flow length into six independent zones. Once liquid enters the ten microchannels of each separated zone, the thermal boundary layer is in developing due to the short flow length, ensuring higher heat transfer coefficient. Such

* Corresponding author. Tel./fax: +86 20 87057656.
E-mail address: xujl@ms.giec.ac.cn (J.L. Xu).

0017-9310/$ - see front matter © 2005 Elsevier Ltd. All rights reserved.
doi:10.1016/j.ijheatmasstransfer.2004.12.008

Nomenclature

A_c	cross-sectional area of each triangular microchannel, m^2
A_w	area of sidewalls of each triangular microchannel, m^2
b	sidewall width of each triangular microchannel, m
C_p	specific heat of water, J/kg °C
D_h	hydraulic diameter of the longitudinal microchannel, m
G	mass flux, kg/m^2 s
f	dimensionless pressure drop
h	heat transfer coefficient, W/m^2 °C
k	thermal conductivity of water, W/m °C
L	length of the longitudinal microchannel, m
L_h	total heating length, m
$L_{h,s}$	flow length for each independent zone, m
L^+	$L^+ = L/(D_h Re)$, non-dimensional microchannel flow length
L_h^+	$L_h^+ = L_h/(D_h \mathrm{Re}\, Pr)$, non-dimensional heating length
$L_{h,s}^+$	non-dimensional heating length for each independent zone
$L_{h,tr}^+$	non-dimensional heating length at which the local Nusselt number reaches 101% of the Nusselt number for the fully thermal developed flow
M	mass flow rate of water, kg/s
N	number of the longitudinal microchannels
N_s	number of the transverse microchannels
Nu	Nusselt number
Nu_s	Nusselt number for the heat sink with the transverse microchannels
Δp	pressure drop across the microchannel heat sink, Pa
Δp_s	pressure drop for the heat sink with the transverse microchannels, Pa
Pr	Prandtl number of water
Q	total heating power received by water, W
q	project heat flux in terms of the effective heating area, W/m^2
R	thermal resistance, °C/W
Re	Reynolds number of water
T	temperature, °C
$T_{chip,max}$	chip maximum temperature of the focused heating area, °C
ΔT_m	mean temperature difference between water and microchannel wall, °C
$\bar{u}$	mean velocity of water, m/s
w	width of each transverse microchannel, m
W	width of the focused heating area, m
x	x coordinate along the streamwise flow direction, m
x^+	$x^+ = x/(D_h Re\, Pr)$, non-dimensional abscissa along the flow direction
y	abscissa perpendicular to the flow direction, m

Greek symbols

v	kinetic viscosity of water
ρ	density of water
ϕ	heat transfer enhancement ratio
η	heat transfer enhancement ratio

Subscripts

c	cross-section
f	liquid water
in	inlet
i	grid in flow direction
j	grid in the width direction
out	outlet
w	wall

thermal boundary layer redeveloping process repeats for all of the six independent zones, thus the overall heat transfer is enhanced. A comparative conventional microchannel heat sink has all of the same sizes except that there are no transverse microchannels.

2. Literature survey on microchannel flow and heat transfer

The objective of this paper focuses on demonstration of the thermal boundary layer redeveloping mechanism that can be incorporated in the microchannel heat sink design. The detailed literature survey of the flow and heat transfer in microchannels is beyond the scope of the present paper, but can be found in some review papers such as [3–5] etc. The literature is becoming rich in microchannel studies. However, as shown, the results are often conflicting, especially considering their performance as compared to classical flow and heat transfer relations. The conflicting results are generally coming from the microchannel fabrication and the measurement methods that are key to determine the flow and heat transfer characteristics [6]. The benchmark data is scarce.

Microscale effects are quite different for gas and liquid flow in microchannels. Rare gas effect occurs if the channel size is down to the same order of the mean

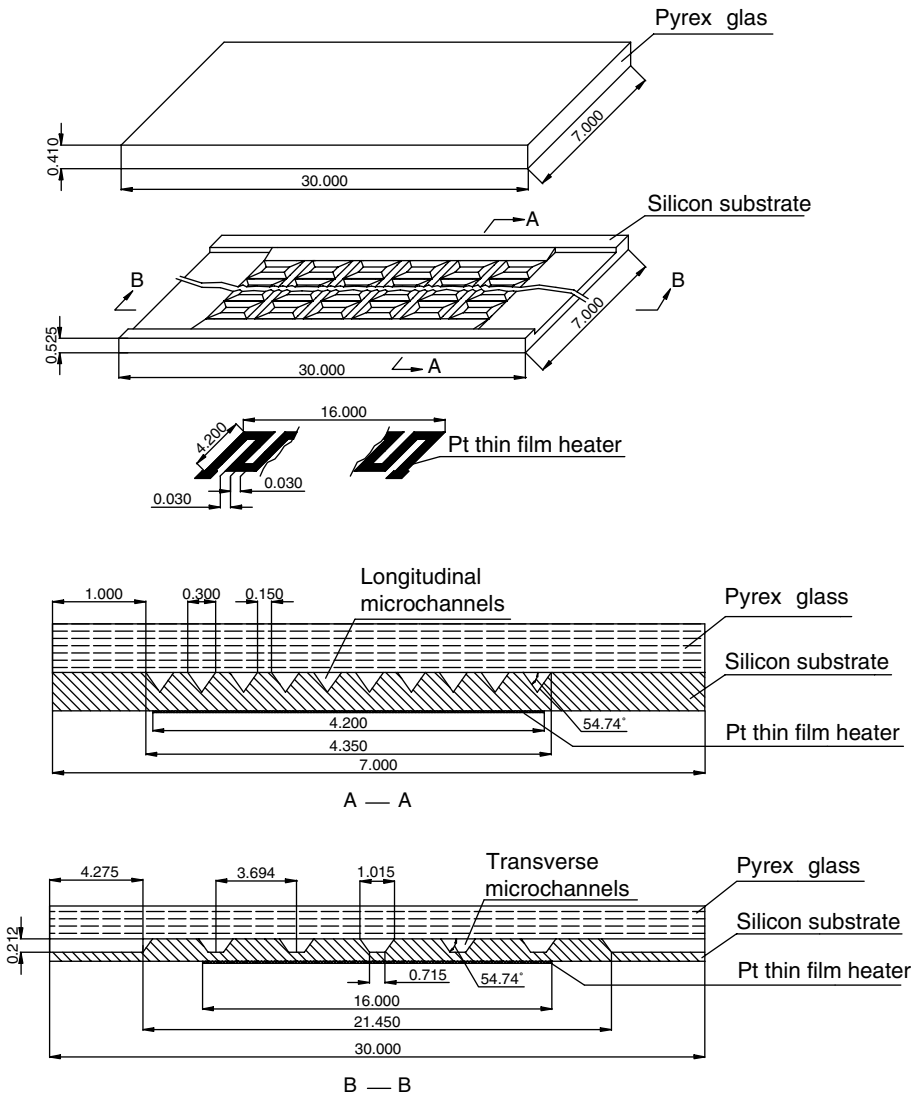

Fig. 1. Silicon heat sink with transverse microchannels (all dimensions are in mm).

free path of the gas. The pressure drop may have a nonlinear distribution along the flow direction due to the compressible effect [7]. Liquids have the densities that may be one thousand times of gas. Liquid molecules are closely packed with each other. Small size down to nano or micron scale may induce the slip boundary condition due to the intermolecular force between solid and liquid particles [8]. In additional to these, any clean liquid may contain metal particles that may induce the electrical-double-layer (EDL) near the solid wall. Pressure-driven liquid flow in microchannels may include the electrical viscous effect [9]. For the microchannel size typically applied in MEMS device between 1 μm and 1.0 mm, the above microscale effects may partially, combined, or not influence the flow and heat transfer because the channel size has so wide range. Up to now it is still difficult to identify the "true" microscale effect from the experiment due to the difficulties in instrumentation.

Very high heat flux chip cooling requires smaller hydraulic diameter and larger flow rate, leading to very high pressure drop. Careful attention should be given to balance the flow and heat transfer for the microchannel heat sink. Fully developed flow and heat transfer assumption is valid for very small channel size. However, when the hydraulic diameter of the microchannels are relative large, such as larger than 100 μm, they have longer "thermal entrance length" to reach the thermal

developed flow. Generally a high heat flux chip may have the length that is several times of the thermal developing length. If we can separate the whole flow length into several independent zones that ensure the thermal developing flow in each independent zone, the overall heat transfer can be enhanced, which can partially compensate the hydraulic diameter effect (generally larger channel size will deteriorate the heat transfer performance). Thus it is possible to use "larger" microchannel size, while the pressure drop is sharply decreased. As noted, most of the available studies were performed for the developed flow of the microchannel heat sinks, very little was conducted on the thermal developing flow in microscale [6]. Moreover, much attention was paid on the improved chip temperature measurements using a high resolution Infrared Radiator Imaging System in this paper.

3. Test section and experimental apparatus

3.1. Description of the microchannel heat sink

Two silicon microchannel heat sinks were fabricated in clean room environment. One is the heat sink incorporating the thermal boundary layer redeveloping concept (Fig. 1) and the other is the conventional one with the same size but without the transverse microchannels.

Both silicon wafers are 30 mm in length, 7 mm in width, 525 μm in thickness. The pyrex glass plate that is bounded with the silicon wafer has the thickness of 410 μm. The whole length of the parallel microchannels in longitudinal direction is 21.45 mm, and the total width coving the ten triangular microchannels is 4.35 mm. The triangular microchannel has the hydraulic diameter of 155 μm A thin platinum film was deposited at the backside of the silicon wafer by "chemical vapor deposition" technique to provide a uniform heat flux. The thin film has the same length of the longitudinal microchannels, but has the total width of 4.20 mm, which is narrower by half triangular microchannel width, to ensure the safe operation of the silicon wafer at extremely high heat flux. The silicon wafer has the effective heating length of 16.0 mm, symmetrical located about the wafer. The heater was connected to a precision AC power supply unit and heat generated in the heater was transferred to the liquid flow from microchannels.

In Fig. 1 five transverse trapezoid microchannels were uniformly arranged in the flow direction, forming six independent zones. The centerline distance between each transverse microchannel is 3.694 mm. Such distance is close to the thermal developing length for the velocity of 1 m/s flowing in triangular microchannels. This configuration design ensures the thermal developing flow in each independent zone thus higher heat transfer performance is obtained covering all of the present experimental data range.

3.2. Experimental setup and procedure

Fig. 2 shows the experimental setup and the corresponding apparatus. Water is pressed by the nitrogen gas and flows successively through a liquid valve, a 2 μm filter, the silicon wafer test section, a heat exchanger, and finally returns to a collection container. The pressure of the water tank is well controlled by adjusting the high precision pressure regulator valve located between the nitrogen gas tank and the water tank. The liquid temperature in the water tank is controlled by a constant temperature control unit (PID control unit) with the uncertainty of ±0.5 °C. In order to decrease the heat loss to the environment and keep the inlet temperature of the test section as the predetermined value, the high quality heat insulation material was wrapped on the outer surface of the connection tube between the outlet of the water tank and the inlet of the test section. The steady water mass flow rate was determined by weighing the mass increment over a longer given period of time using a high precision electronic balance, which has the accuracy of 0.02 g. The inlet and outlet temperatures were measured by the high precision jacket thermocouples with the diameter of 1.0 mm. These thermocouples have the measurement errors within ±0.3 °C. The inlet fluid pressure was measured by a Setra pressure transducer (Model 206), which was calibrated against a known standard and the uncertainty in the pressure measurements was less than 1%. All of the pressure and temperature signals were collected by a HP data acquisition system. At the top of the silicon wafer, a microscope (Leica series, Germany) was installed to monitor the flow status through the microchannels. This is important to keep the single-phase liquid flow in microchannels at high heat fluxes. Boiling is never initiated.

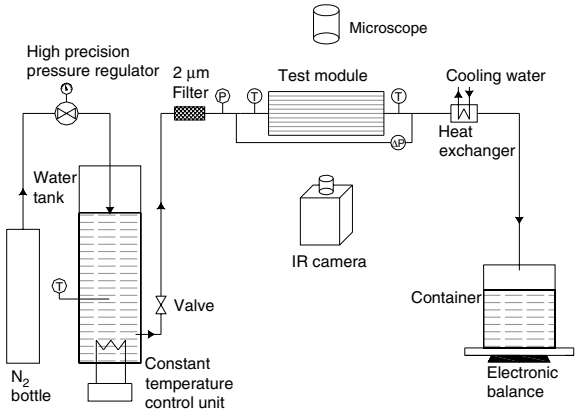

Fig. 2. Experimental setup and apparatus.

3.3. Chip temperature measurement

Distinct with other studies, the wafer temperatures of the backside thin film were measured by a high resolution, high accuracy Infrared Radiator Imaging System (FLIR ThermaCAM SC3000 IR). This system has a thermal sensitivity of 0.02 °C at 30 °C, a spatial resolution of 1.1 mrad, a typical resolution of 320×240 over the focused area, and an image frequency of 50 Hz, allowing precise determination of the temperature gradients across the chip surface.

Throughout all of the tests, the IR camera was situated so that the heating area of the silicon wafer (16.0×4.2 mm^2) is in the field of view. Using this technique, the temperature gradient, the maximum temperature and the transient response could be detected. The IR Imaging System was connected to a PC. For each run case, the PC stores the image file and the corresponding data file which contains 6080 data points related to the focused thin film heating area.

The measurement of temperature by means of the radiation power emitted from a surface requires a careful calibration of the emissivity, which depends strongly on the surface topography and the wavelengths that are interrogated [10]. The spatial resolution is limited to the working wavelength of the IR camera that is cantered in one of the atmospheric windows 8–9 μm. The ThermaCAM SC3000 has a GsAs, Quantum Well Infrared Photon FPA detector working in the spectral range of 8–9 μm.This is the physical limitation. We use an addition microlens over the IR camera, forming the real spatial resolution of 17.5 μm. A very thin "black lacquer" was uniformly coated on the thin film surface of the silicon wafer. An emissivity of approximately 0.94 resulted in good measurement accuracies. The temperature dependence of emissivity within the considered range can be neglected. Such procedure is similar to that of Hapke et al. [11]. Using this technique, the IR Imaging System was calibrated against a set of known standard temperatures with the accuracy of 0.3 °C.

It is noted that the measured surface temperature is strongly depended on the emissivity. Other factors, such as the ambient temperature, the air humidity and the distance between the camera lens and the silicon wafer that are put into the software have little influences. Because the black paint is only focused on the effecting heating area, there is a stiff emissivity change at the heating element boundaries. The IR camera sees more area larger than that of the heating element thus poor readings are obtained with the area beyond the effective heating surface due to that the "bright" thin Pt film with lower emissivity is directly exposed in the camera view. However, these poor readings are not used for the data process. We are only interested in the temperature readings within the painted heating area.

The experiment covers the following ranges: inlet pressures of 1–2 bar, pressure drops of 10–100 kPa, inlet temperatures of 30–70 °C, mass fluxes of 534.79–4132.85 kg/m^{2}s, and the project heat fluxes of 10–100 W/cm^2, which is defined as the total heating power that is received by the liquid divided by the effective heating area. Deionized water is used as the working fluid.

4. Data reduction

4.1. Dimensionless pressure drop

The data reduction procedure is similar to Wu and Chen [12]. It is convenient to use the dimensionless pressure drop in this paper instead of the friction factor, while the later is usually defined for the fully developed and uninterrupted flow. They have the same form expressed as

$$f = \Delta p \cdot \frac{D_h}{L} \cdot \frac{1}{2\rho \bar{u}^2} \tag{1}$$

where Δp is the pressure drop measured by the pressure drop transducer across the microchannel heat sink, ρ is the liquid density in terms of the mean value of the inlet and outlet temperatures, D_h and L are the hydraulic diameter and the whole length of the longitudinal microchannels, and $\bar{u}$ is the average velocity of water.

Using the measured mass flow rate of water, M, the dimensionless pressure drop is rewritten as

$$f = \frac{\Delta p D_h \rho N^2 A_c^2}{2LM^2} \tag{2}$$

where A_c is the cross-sectional area of each triangular microchannel, N is the number of the longitudinal microchannels.

4.2. Overall heat transfer coefficient

The overall heat transfer coefficient for the deionized water flowing through the longitudinal microchannels is defined as

$$h = \frac{Q}{NA_w \Delta T_m} \tag{3}$$

where A_w is the total area of the side walls of longitudinal microchannels. The pyrex glass is assumed to have an adiabatic condition. Q is the heating power that is received by water, which is calculated by the energy conservation equation from the inlet to outlet liquid temperatures. Using the powermeter readings as the power input results in uncertainties which maybe different from case to case. The heat extracting efficiency η is

defined as Q divided by the total heating power. Covering the present data range η is in the range of 90% to 96%. It acquires the lower range for the lower heating power and higher end for the higher heating power, considering the total heat loss to the environment.

The mean temperature difference ΔT_m between the channel wall and the water is calculated by

$$\Delta T_m = \overline{T}_w - \frac{1}{2}(T_{in} + T_{out}) = \frac{\sum_{i=1}^{152}\sum_{j=1}^{40} T_{ij}}{6080} - \frac{1}{2}(T_{in} + T_{out}) \quad (4)$$

where $\overline{T}_w$ is the average wall temperature, T_{ij} is the chip local temperature measured by the IR Imaging System at each point in the heating area (black painted area). The heating area totally forms 6080 data points, i is the longitudinal grid and j is the transverse grid. Totally there are 152 grids for i direction and 40 grids for j direction. For simplicity, the temperature differences between the thin film and the side wall of the microchannels is neglected due to the very large thermal conductivity of the silicon wafer. T_{in} and T_{out} are the inlet and outlet bulk temperatures of water.

The average Nusselt number in terms of various measurements is written as

$$Nu = \frac{MC_pD_h(T_{out} - T_{in})}{NkA_w\Delta T_m} \quad (5)$$

where C_p and k are the specific heat and the thermal conductivity of water. The mean temperature of water $(T_{in} + T_{out})/2$ was used to characterize the physical properties of water, including ρ, v, k, and C_p, which are assumed to be independent of pressure. In order to perform the comparative analysis between the wafer heat sinks with and without the transverse microchannels, the data reduction follows the same procedures for the two heat sinks.

4.3. Local heat transfer coefficient

The local heat transfer coefficients and Nusselt numbers are obtained in terms of local temperatures in x–y coordinates

$$h(x,y) = \frac{Q}{NA_w(T_w(x,y) - T_f(x))} \quad (6)$$

$$Nu(x,y) = \frac{h(x,y)D_h}{k} \quad (7)$$

In Eq. (6), the local liquid temperature T_f is assumed to have a linear distribution along the flow direction. The local Nusselt number in terms of various measurements finally yields:

$$Nu(x,y) = \frac{MC_pD_h(T_{out} - T_{in})}{NA_wk(T_w(x,y) - T_f(x))} \quad (8)$$

Table 1
Measurement errors

Parameters	Maximum errors	Parameters	Maximum errors
D_h	1.29%	Δp	0.1%
L	0.01%	T	0.5 °C (1.67%)
L_h	0.01%	ΔT_m	1.67%
A_c	1.15%	Re	2.96%
A_w	0.77%	f	3.33%
M	1.02%	Nu	2.93%

4.4. Error analysis

In terms of Eqs. (2), (5) and (8), the errors accounting for f, Nu, and $Nu(x,y)$ come from the measurement errors of a set of parameters, that are listed in Table 1. Performing the standard error analysis [13], the maximum uncertainties in determining these parameters are given in Table 1. It is seen that the maximum errors due to the measurements are less than 3.33%, 2.93%, 2.93% for f, Nu and $Nu(x,y)$ respectively. Even though all the temperatures measured by the thermocouples and the IR camera are carefully calibrated, the maximum errors of 0.5 °C are used for the error analysis. Normalizing such error with respect to the minimum inlet liquid temperature such as 30 °C yields the maximum possible error of 1.67% for the temperatures.

5. Experimental results and discussion

5.1. Chip temperature and Nusselt number distribution for the conventional heat sink

A typical run case for the project heat flux high up to 104 W/cm^2 is shown in Fig. 4, in which Fig. 4a–c are for

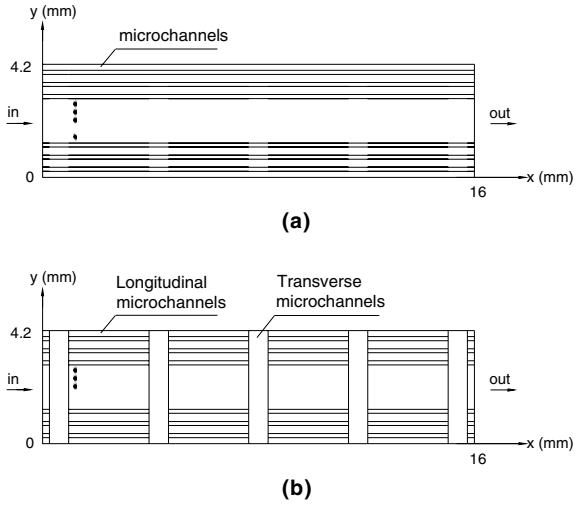

Fig. 3. Coordinates attached on the focused heating area (all dimensions are scaled).

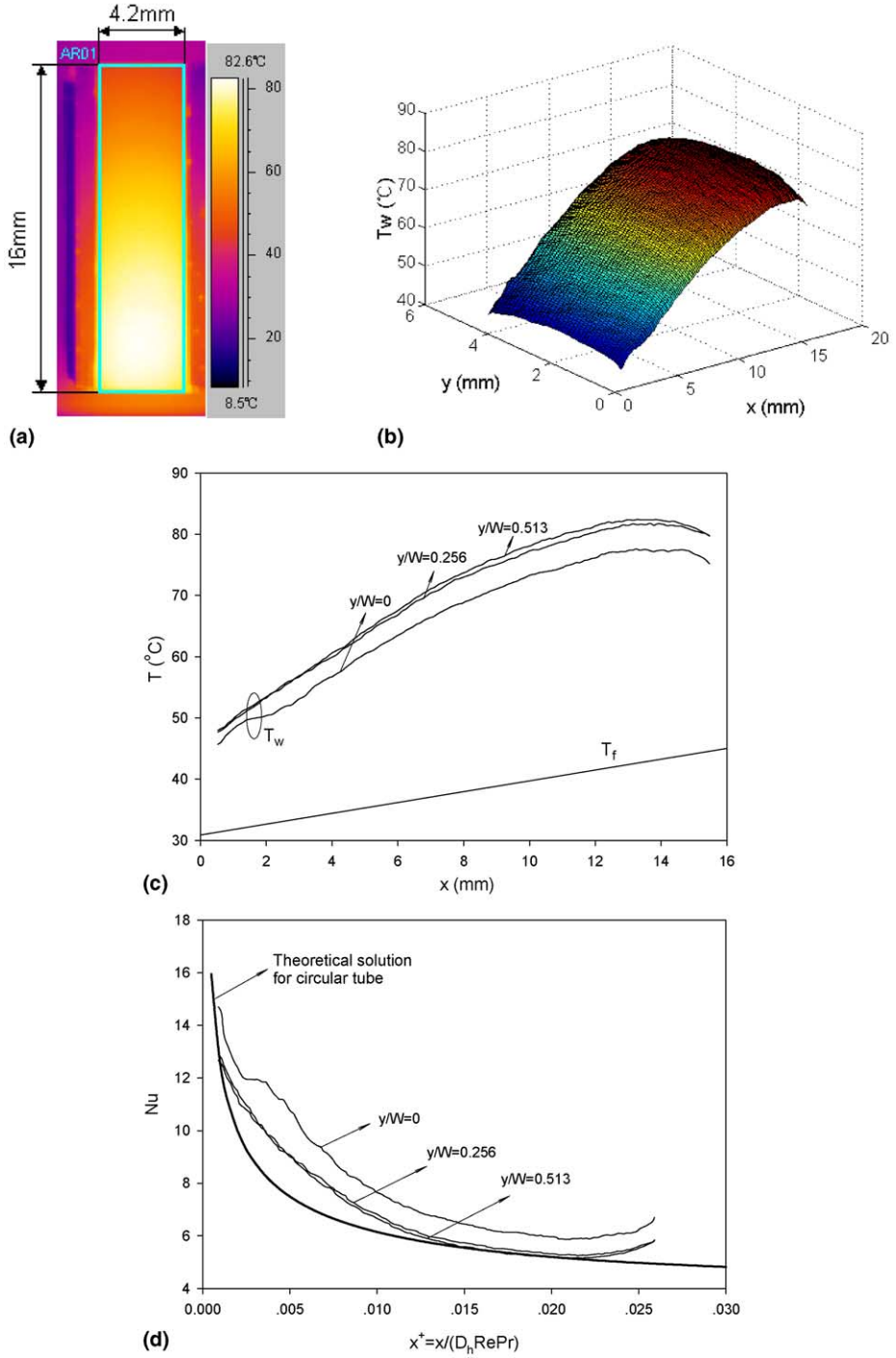

Fig. 4. Chip temperatures and local Nusselt numbers for the conventional heat sink (T_{in} = 30.9 °C, Q = 69.7 W, G = 3705.8 kg/m^{2}s, Δp = 99.8 kPa, Re = 871, q = 104 W/cm^2; (a) IR color image for the temperatures; (b) three-dimensional temperatures; (c) chip temperatures versus flow length and (d) Nusselt numbers versus flow length).

the chip temperature distributions, Fig. 4d for the Nusselt number distributions. The fully developed hydraulic flow is maintained due to the Prandtl number much greater than unity. However, the thermal developing

flow is maintained because $L_h^+ = 0.0275$ which is only half of the transition value of $L_h^+ = 0.05$ at which the thermal developed flow is approached [14].

The color IR image (Fig. 4a) intuitionisticly illustrates the chip temperature and its gradient in x–y plane of the focused heating area. The temperatures in a three-dimensional form shown in Fig. 4b behave the "horseback" shape with apparent positive gradient in x-direction but slight gradient in y-direction. It is seen that the chip temperature along the flow direction is not linear. The temperature difference between the chip and the liquid is increased with increasing x but reaches the maximum value at $x = 14$ mm, close to the end of the heating area at $x = 16$ mm. A slight negative gradient is observed from $x = 14$ mm to $x = 16$ mm, attributed to the thermal conduction in solid silicon near the end of the heating area in x-direction. The chip temperatures are slightly higher at the chip center region (little differences were identified between $y/W = 0.256$ and $y/W = 0.513$). But they are slightly lower at $y = 0$ (the margin of the heating location), also attributed to the thermal conduction in solid silicon in y-direction. The temperature difference between $y/W = 0$ and $y/W = 0.513$ is about 4–5 °C.

As observed in Fig. 4d the following phenomena could be identified: (1) The Nusselt numbers are much higher at the "entrance region". The thermal developing region is longer than half of the total heating length. (2) The Nusselt numbers are higher at the margin of the heating area at $y/W = 0$ and $y/W = 1$, corresponding to the lower temperatures at these locations due to the thermal conduction in solid silicon. (3) A very slight positive gradients of the Nusselt numbers occur at the end of the heating area ($x/L_h = 1$), also due to the thermal conduction in the solid silicon. (4) The Nusselt Numbers approach uniform in the center of the heating sera in y-direction. For instance, they tend to collapse to a single curve at $y/W = 0.256$ and $y/W = 0.513$.

When $x^+ > 0.013$, the local Nusselt numbers at the chip center region can match the theoretical solution for the circular tube at the constant heat flux condition in macroscale predicted by [14].

It is noted that for the flow and heat transfer analysis at high heat flux conditions, careful attentions should be given on the liquid property variations. Under such conditions if the liquid temperatures increase 20 °C, the liquid Prandtl number decreases by 35% from 30 °C to 50 °C, which affects the development of the thermal boundary layer. In terms of the present experimental observations, the future numerical modelings should include the whole silicon wafer as the calculation domain, and account for the liquid physical property variations. Flow and heat transfer in all of the microchannels shall be coupled with the whole silicon wafer.

For all of the case tested, the measured parameters are exactly symmetry about the centerline of $y/W = 0.5$ This is also true for the new microchannel heat sink.

5.2. Chip temperature and Nusselt number distribution for the heat sink with transverse microchannels

Verifying Figs. 4 and 5a–d, the chip temperatures and Nusselt numbers have the following similar behaviors for both heat sinks with and without the transverse microchannels: (1) Non-linear distribution along the flow length. (2) Parameter gradients occur at the margins of $y/W = 0$, $y/W = 1$, $x/L_h = 0$, and $x/L_h = 1$, due to the thermal conduction in solid silicon at the junction between the heated and the un-heated area. However, the chip temperatures and Nusselt numbers for the heat sink with the transverse microchannels display the cycle behavior along the flow length (see Fig. 5a–d), supporting the periodic thermal boundary layer redeveloping concept. Note in Fig. 3b that there are four independent zones in the focused heating area. Thus four cycles of the chip temperatures and Nusselt numbers along the flow length occur. At the four transverse trapezoid microchannel regions, four thin horizontal "brighter line" can be identified (see Fig. 5a), resulted from the smaller flow velocity in the transverse microchannels. Narrow the width of the transverse trapezoid microchannel and increase the thickness of the silicon wafer can definitely reduce or release such local temperature gradient and the corresponding thermal stress.

In Fig. 5d, it is shown that the first zone has larger Nusselt numbers. The second, third and fourth zones repeat the very similar distributions. Each cycle of the Nusselt number corresponds to each independent zone. The smaller flow velocity in the trapezoid microchannel induces smaller Nusselt number. But they have a step increase once liquid reenters the parallel longitudinal microchannels, followed by a slow decrease until the liquid enters the next transverse microchannel. The relative short length of the thermal boundary layer $L_{h,s}^+$ for each independent zone provides higher Nusselt numbers.

5.3. Comparisons between the two microchannel heat sinks

5.3.1. Heat transfer enhancement of the new microchannel heat sink

In order to further identify the benefits that we can obtain from the new microchannel heat sink, a pair of comparative run cases are given in Fig. 6a–d, which are based on the similar flow conditions for both heat sinks, with same inlet liquid temperature of 30 °C, effective heating power of 70 W and mean flow velocity of 3.2 m/s. The color IR images (see Fig. 6a–b) intuitionisticly illustrate that the new heat sink lowers the chip temperatures. The chip temperatures and the Nusselt Numbers show smaller differences between the two wafers in the first zone. However, the new heat sink can decrease the temperatures by 14 °C maximally in

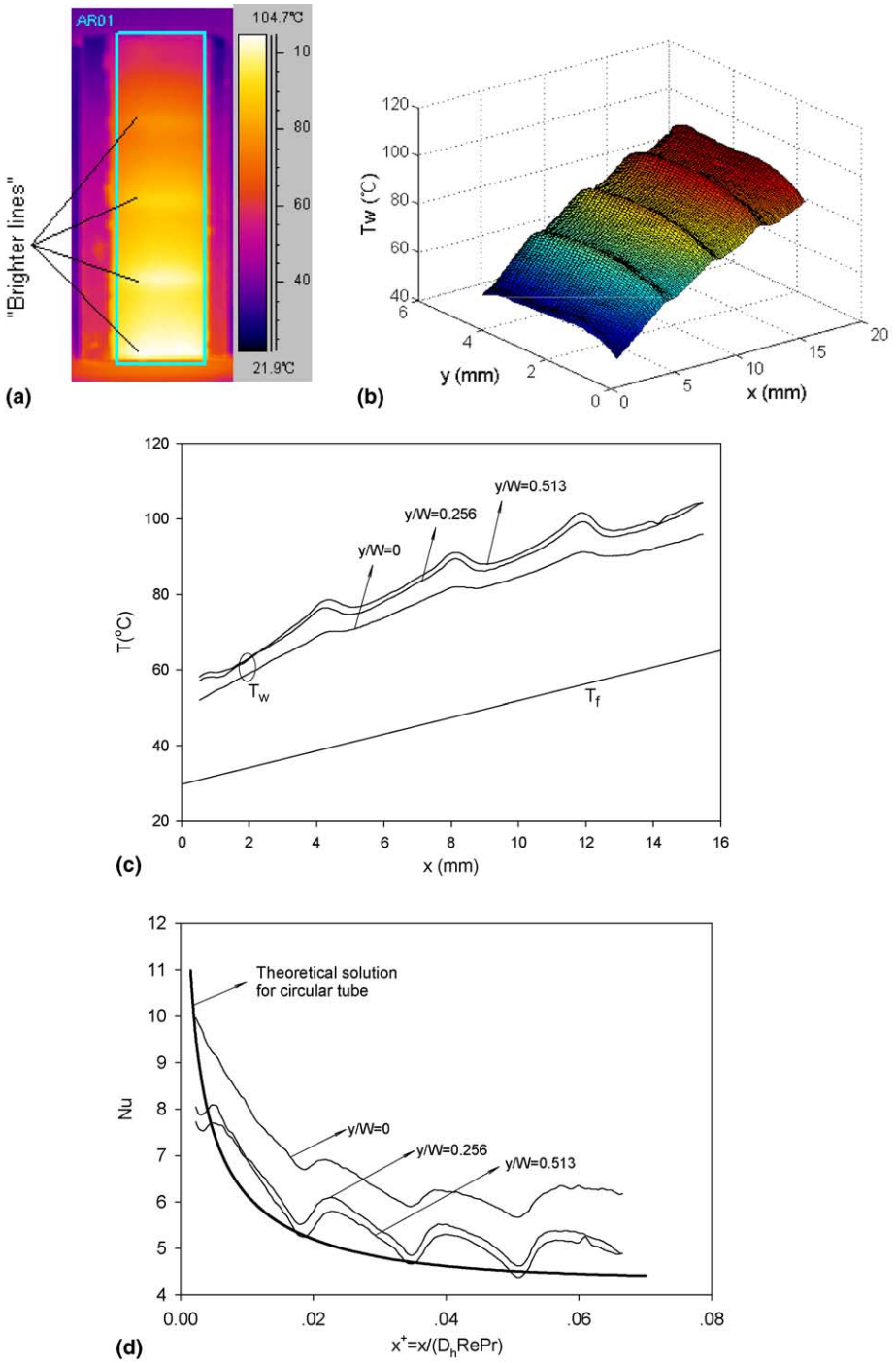

Fig. 5. Chip temperatures and local Nusselt numbers for the new heat sink (T_{in} = 29.8 °C, Q = 69.1 W, G = 1469.3 kg/m^2 s, Δp = 20.2 kPa, Re = 345, q = 103 W/cm^2; (a) IR color image for the temperatures; (b) three-dimensional temperatures; (c) chip temperatures versus flow length and (d) Nusselt numbers versus flow length).

other regions. The Nusselt numbers, which are higher for the new heat sink, display the cycle behavior for the four independent zones. In each independent zone, the Nusselt numbers are lower in the transverse microchannel regions, but will have a sharp increase followed by a slow decrease. The overall Nusselt number for the

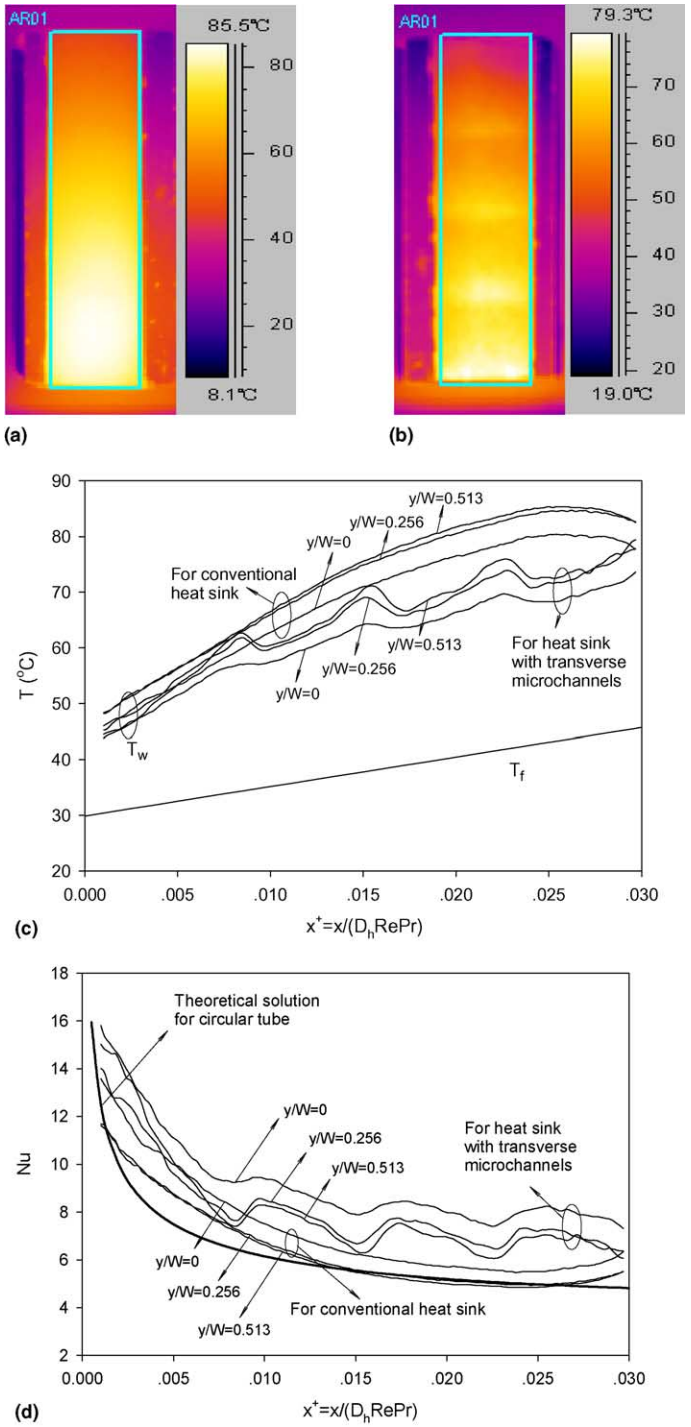

Fig. 6. Comparisons between two heat sinks: (a) for conventional heat sink T_{in} = 29.5 °C, Q = 69.8 W, G = 3216.9 kg/m^2 s, Δp = 82.2 kPa; (b) for new heat sink, T_{in} = 29.8 °C, Q = 69.8 W, G = 3238.9 kg/m^2 s, Δp_s = 60.3 kPa; (c) chip temperatures along the flow length for the two heat sinks; and (d) Nusselt numbers along the flow length for the two heat sinks.

new heat sink is 7.954, which is increased by 26.4% compared with the conventional one. For all of the run cases tested, even though the chip temperatures are higher relative to the neighboring region in the transverse

microchannel regions, but they are still quite lower than those in the corresponding regions for the conventional heat sink.

For a given geometry design of the new heat sink, the heat transfer enhancement is controlled by the dimensionless parameter, $L^+_{h,s} = L_{h,s}/(D_h Re Pr)$, for each independent zone. Neglecting the total widths of the transverse microchannels, we have

$$L^+_{h,s} = L^+_h/(N_s + 1) \tag{9}$$

Theoretically the heat transfer enhancement ratio ϕ is defined as the overall Nusselt number for the new heat sink divided by that for the conventional one without the transverse microchannels:

$$\phi = \frac{Nu_s}{Nu} = \frac{(N_s + 1)\int_0^{L^+_{h,s}} Nu\, dx^+}{\int_0^{(N_s+1)L^+_{h,s}} Nu\, dx^+} \tag{10}$$

Fig. 7 demonstrates the higher overall Nusselt numbers for the new heat sink than for the conventional one. The conventional triangular microchannels can match the theoretical solution of the circular tube in macroscale [14].

Note that Fig. 7 is obtained using the non-dimensional parameters of Nusselt numbers and effective heating length. The curve for the conventional microchannels can be extended to other microchannel arrays, providing that the hydraulic diameter of the microchannel is larger enough such as more than 100 μm thus the possible microscale effects can be neglected. The varied physical properties are considered because the curve is experimental determined. However, the curve of the Nusselt numbers versus the non-dimensional effective heating length is only for the new microchannel arrays with the heating length crossing five transverse channels

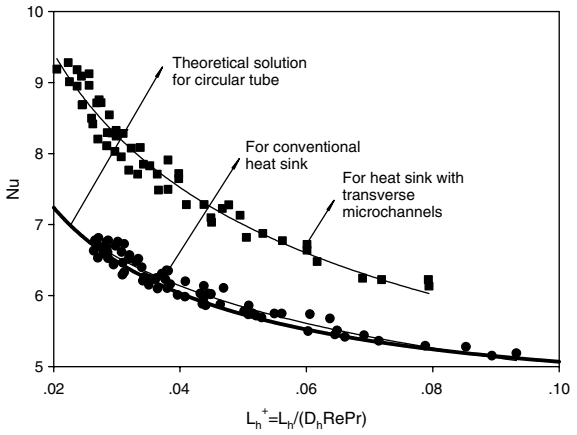

Fig. 7. Overall Nusselt number versus L^+_h (correlation for conventional heat sink: $Nu = 3.0045(L^+_h)^{-0.2220}$, 72 data points, error < 3.70%; correlation for the new heat sink: $Nu = 2.6614(L^+_h)^{-0.3228}$, 54 data points, error < 5.01%).

over four independent zones in which the thermal boundary layer is developing. Future numerical/experimental studies will be focused on the heat transfer performance for the microchannel arrays with different transverse channels.

The experimental decided heat transfer enhancement ratio in terms of data illustrated in Fig. 7 is in the range of 1.31–1.12 within the non-dimensional heating length L^+_h of 0.02–1.10. It is noted that the net heat transfer enhancement ratio consists of two mechanisms, one is the thermal boundary layer redeveloping effect and the other is the wet heat transfer area increase effect. For the present microchannel array with transverse channels, the heat transfer area is increased by 10.8% from the conventional microchannel heat sink of 83.2 mm^2 to the new microchannel heat sink of 92.2 mm^2 within the effective heating length of 16.0 mm. Therefore, the net heat transfer enhancement ratio for the new microchannel heat sink due to the thermal boundary layer redeveloping effect is from 1.202 to 1.01. At the lower end of the heat transfer enhancement ratio, the new heat sink is approaching the developed thermal boundary layer.

5.3.2. Pressure drop reduction of the new microchannel heat sink

For the comparative run cases shown in Fig. 6, the new microchannel heat sink decreases the pressure drop by 27%. The very small flow velocity in the transverse microchannels leads to the neglected pressure drops across the width of the transverse trapezoid microchannels. Assuming the linear distribution of the pressure drop versus the flow length for the hydraulically developed flow, the total pressure drops for the two heat sinks have the following relationship

$$\Delta p_s = (L - N_s \cdot w)\Delta p/L \tag{11}$$

Here L is the whole flow length of the longitudinal microchannel, N_s and w are the number and the width of the transverse trapezoid microchannels, Δp_s and Δp are the pressure drops for the new heat sink and the conventional one, respectively. In Eq. (11) $L - N_s \cdot w$ is the "effective flow length" for the new microchannel heat sink. In terms of the geometry parameters, the pressure drop for the new heat sink should be decreased by 26% compared with the conventional one based on Eq. (11). Such simple estimation of the pressure drops related to the two microchannel heat sinks conforms the measured values well.

Fig. 8 illustrates the decreased dimensionless pressure drops for the new heat sink than for the conventional one, as expected. At lower Reynolds numbers such as less than 300, the dimensionless pressure drops for the conventional triangular microchannels are very close to those for the circular tube. However, at higher Reynolds numbers, the dimensionless pressure drops are larger than those of the circular tubes. Such differ-

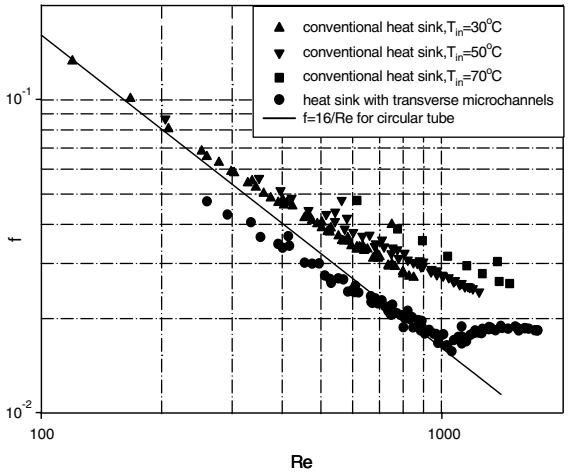

Fig. 8. Dimensionless pressure drops versus the Reynolds numbers for two microchannel heat sinks.

ences become larger with increasing the Reynolds number. The dimensionless length $L^+ = L/(D_h Re)$ is shortened with increasing Re, resulting in that the hydraulic boundary layer may not be fully developed. This is the possible explanation of such deviations. Also can be seen in Fig. 8 is that the inlet liquid temperatures can affect the dimensionless pressure drops for the conventional triangular microchannels. Higher inlet liquid temperatures lead to slight higher dimensionless pressure drops, possibly due to the physical property variations at high heat flux conditions. For all of the cases tested in the present paper, the transition from the laminar flow to the turbulent flow is not observed for the conventional heat sink. It is noted that such transitions occur at the Reynolds numbers between 1000 and 1100 for the new heat sink, indicating that the enhanced liquid mixing in the transverse microchannels leads to the earlier transition from laminar flow to turbulent flow. Harms et al. [6] observed that the transition from laminar flow to turbulent flow occurs at the critical Reynolds number of 1500 for the multiple rectangular microchannels with 300 μm in width and 1000 μm in depth. Such transition Reynolds number is lower than the value of 2400 rectangular channels in macroscale. Harms et al. [6] stated that the severity of the inlet condition is known to have a significant effect on the critical Reynolds number. The smaller Reynolds number at which the transition occurs observed for the new microchannel heat sink agrees with the previous studies [6] qualitatively. For the new heat sink, all of the run cases share a single curve of the dimensionless pressure drops. The effects of the inlet liquid temperature are not observed.

Plotting the pressure drop against the thermal resistance is the best way to compare heat transfer systems because these are the competing factors in any practical design. One should be aware that the definition of the thermal resistance is not unique among various investigators. Many researchers define the characteristic temperature difference as the inlet liquid temperature and the maximum heater temperature. The present paper follows such definition. Thus the thermal resistance is written as

$$R = \frac{T_{\text{chip,max}} - T_{\text{in}}}{Q} \tag{12}$$

As shown in Fig. 9, the new microchannel heat sink can significantly reduce the thermal resistances. For the conventional microchannel heat sink the thermal resistances tend to collapse to a single curve. However, for the new microchannel heat sink, they do not follow the single curve for $R < 0.8$ °C/W. Such deviations are decreased with increasing the thermal resistances.

5.4. Design consideration and prospective of the new microchannel heat sink

For a practical design of the new heat sink, the $L^+_{h,s}$ for each independent zone is suggested to be $cL^+_{h,tr}$. Here c is suggested from 0.5 to 1.0, $L^+_{h,tr}$ is the dimensionless heating length at which the local Nusselt number reaches 101% of the Nusselt number for the fully thermal developed flow. If $c = 0.5$ is used, the overall Nusselt number can be 1.46 times of the fully developed value, neglecting the possible "microscale effect". At a given total flow length, smaller $L^+_{h,s}$ for each independent zone leads to higher heat transfer performance, but more transverse microchannels are needed. Optimization of the new microchannel heat sink is expected in the near future.

In macroscale, heat transfer enhancement using any technique may accompany the pressure drop increase. In microscale, heat transfer enhancement can be obtained by decreasing D but Δp is greatly increased. The

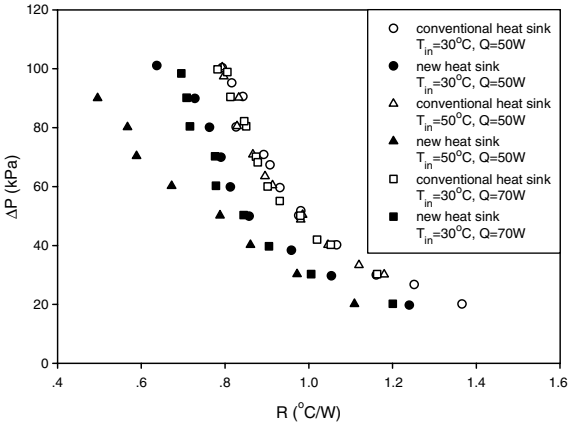

Fig. 9. Pressure drops versus the thermal resistances for the two microchannel heat sinks.

new microchannel heat sink not only enhances heat transfer but also decreases the pressure drop, ensuring the possibility of using "larger" microchannel hydraulic diameter such as more than 100 μm.Thus the microchannel heat sink may not be plugged easily and less pumping power is needed. The pressure drop decrease phenomenon while enhancing heat transfer is attractive for the semiconductor devices, especially for very high heat flux. The new microchannel heat sink is simple in structure and can be fabricated in typical clean room environment. The potential versatility of this system can be further optimized by additional experimental/numerical works in microscale.

6. Conclusions

A set of experiments were performed for the microscale heat transfer enhancement using the thermal boundary layer redeveloping concept. The following conclusions can be drawn:

1. For the conventional triangular microchannel heat sinks, the chip temperature versus the flow direction is not linear, behaving the "horseback" shape. The "thermal entrance length" can be longer than half of the total heating length. The maximum chip temperature occurs just upstream of the ended heating length. Apparent temperature gradients occur at the margins of the focused heating area, due to the thermal conduction in the solid silicon.
2. Correspondingly, the Nusselt numbers are higher at the "thermal entrance region". Slight positive gradients appear at the end of the heating area, due to the thermal conduction in solid silicon. Generally the local Nusselt numbers in the center region of the focused heating area can match the classical theoretical solutions for the circular tube in macroscale.
3. The heat sink with transverse microchannels also has the non-linear distributions of temperatures and Nusselt numbers. Parameter gradients appear at the margins of the selected heating area. Besides, the parameters show the cycle behavior. In each independent zone, the Nusselt number is lower in the transverse microchannel region, but will have a sharp increase followed by a slow decrease. The heat transfer is indeed enhanced due to the thermal boundary layer redeveloping mechanism.
4. The new microchannel heat sink can significant reduce the pressure drops while enhancing heat transfer, resulted from the shortened "effective flow length". The new structure may lead to the earlier transition from laminar flow to turbulent flow.
5. Eq. (10) can be used to evaluate the heat transfer enhancement ratio, qualitatively. The dimensionless number $L^{+}_{h,s}$ is selected as the control parameter for the design consideration.
6. The boundary layer redeveloping concept can be further extended to other flow systems in microscale. Optimization of the new heat transfer device is expected in the near future.

Acknowledgement

This work is supported by the National Natural Science Foundation of China (50476088), Natural Science Foundation of Guangdong Province (32700) and the Science and Technology Development Foundation of Guangdong Province (33103).

References

[1] A.C. Lyman, R.A. Stephan, K.A. Thole, L.W. Zhang, S.B. Memory, Scaling of heat transfer coefficients along louvered fins, Exp. Thermal Fluid Sci. 26 (2002) 547–563.
[2] M.E. Springer, K.A. Thole, Entry region of louvered fin heat exchangers, Exp. Thermal Fluid Sci. 19 (1999) 223–232.
[3] B. Palm, Heat transfer in microchannels, Microscale Thermopys. Eng. 5 (2001) 155–175.
[4] N.T. Obot, Toward a better understanding of friction and heat and mass transfer in microchannels—a literature review, Microscale Thermophys. Eng. 6 (3) (2002) 155–173.
[5] Z.Y. Guo, Z.X. Li, Size effect of microscale single-phase flow and heat transfer, Int. J. Heat Mass Transfer 46 (2003) 149–159.
[6] T.M. Harms, M.J. Kazmierczak, F.M. Gerner, Developing convective heat transfer in deep rectangular microchannels, Int. J. Heat Fluid Flow 20 (1999) 149–157.
[7] M. Gad-el-Hak, The fluid mechanics of microdevices—the Freeman scholar lecture, ASME, J. Fluids Eng. 121 (5) (1999) 5–33.
[8] P.A. Thompson, S.M. Troian, A general boundary condition for liquid flow at solid surfaces, Lett. Nature 389 (25) (1997) 360–362.
[9] T.S. Zhao, Q. Liao, Thermal effects on electro-osmotic pumping of liquids in microchannels, J. Micromech. Microeng. 12 (2002) 962–970.
[10] G.A. Bennett, S.D. Briles, Calibration procedure developed for IR surface-temperature measurements, IEEE Trans. Components Hybrids Manufact. Technol. 12 (1989) 690–695.
[11] Hapke, H. Boye, J. Schmidt, Onset of nucleate boiling in minichannels, Int. J. Thermal Sci. 39 (2000) 505–513.
[12] H.Y. Wu, P. Cheng, An experimental study of convective heat transfer in silicon microchannels with different surface conditions, Int. J. Heat Mass Transfer 46 (2003) 2547–2556.
[13] R.J. Moffat, Describing the uncertainties in experimental results, Exp. Thermal Fluid Sci. 1 (1988) 3–17.
[14] W.M. Kays, M.E. Crawford, Convective Heat and Mass Transfer, second ed., McGraw Hill, New York, 1980.